Multi-wire arc additive manufacturing of TC4/Nb bionic layered heterogeneous alloy: Microstructure evolution and mechanical properties

P.F. Jiang [a], M.H. Nie [a], J.Z. Teng [a], X.B. Wang [b], C.Z. Liu [c], Z.H. Zhang [a,*]

[a] Key Laboratory of Bionic Engineering, (Ministry of Education), College of Biological and Agricultural Engineering, Jilin University, 5988 Renmin Street, Changchun, 130025, PR China
[b] Key Laboratory for Liquid-Solid Structural Evolution and Processing of Materials (Ministry of Education), Shandong University, Jingshi Road 17923, Jinan, 250061, PR China
[c] Institute of Orthopaedic & Musculoskeletal Science, University College London, Royal National Orthopaedic Hospital, Stanmore, London, HA7 4LP, UK

ARTICLEINFO

Keywords:
TC4/Nb alloy
Multi-material structure
Multi-wire arc additive manufacturing
Microstructure evolution
Mechanical properties

ABSTRACT

The performance improvement of wire arc additive manufacturing component relies on structural innovation and tailored printing, and the naturally optimized structure can provide inspiration for design and manufacturing. In this work, a layered TC4/Nb multi-material alloy component inspired by the biological structure of the Crysomallon squamiferum shell was designed and fabricated by multi-wire arc additive manufacturing (MWAAM). The interfacial reaction, phase composition, microstructure evolution, crystal growth, mechanical properties and crack propagation of MWAAM-processed bionic heterogeneous TC4/Nb multi-material alloy component were investigated by EDS, SEM, EBSD and mechanical tester. The results indicated that the good metallurgical bond was formed between the different layers of MWAAM TC4/Nb multi-material alloy sample. The Ti/Nb multi-material alloy component was mainly composed of α-Ti, β-Ti and (Nb, Ti) solid solution phases. The morphology of phase underwent a continuous transformation process from TC4 layer to G1 layer with the increase of Nb content: Lamellar α + β →Thin lamellar α + Short rod α + β → Acicular α + β → Thin acicular α + β. In addition, the grain size of TC4/Nb multi material alloy component from TC4 layer to G2 layer gradually from 3.534 μm decreased to 2.904 μm with the increase of Nb content. The microhardness of TC4/Nb multi-material alloy from TC4 layer to G2 layer ranged from 404.04 HV to 245.23 HV. The relatively high compression strength and ultimate tensile strength of TC4/Nb multi-material alloy sample were 2162.64 ± 26 MPa and 663.39 MPa, and corresponding strain were 31.99% and 17.77%, respectively. The excellent mechanical behavior was mainly contributed to the excellent combination of gradient transition of grain size and microstructure evolution between layers. Crack propagation was mainly dominated by crack deflection and multistage cracking during the tensile test process. The strength of TC4 layer was the highest than G1 and G2 layer in the TC4/Nb multi-material alloy component.

1. Introduction

Since ancient times, learning from biological simulation had become an eternal theme in the development of science and technology. After billions of years of evolution and optimization, biological multi-scale structure had been equipped with special capabilities far superior to human design [1]. Biomimetic technology is widely used in aerospace, energy and other scientific and technological innovation fields [2]. With the lowest material and energy consumption and the most accurate use of information, organisms achieve the best adaptability to the environment and accurate self-regulation ability [3,4]. As a special deep-sea creature that lives at hydrothermal vents in the Indian Ocean at a depth of 2700 m, the Crysomallon squamiferum is able to withstand the heat and corrosive liquids spewing from undersea vents and can resist natural enemies [4]. Its unique function was mainly attributed to the natural armor of the iron-plated multilayer structure of the Crysomallon squamiferum. The shell of snail is reported to have three layers, from the outside to the inside: an iron-bearing outer layer, a thick organic middle layer, and a hard calcified inner layer. In addition, the inner layer contains gradient layer (GL), cross lamellar layer (CLL) and prismatic layer (PL) structures, as shown in Fig. 1. This special structure made the shell of the Crysomallon squamiferum significantly better than the shell

* Corresponding author.
E-mail address: zhzh@jlu.edu.cn (Z.H. Zhang).

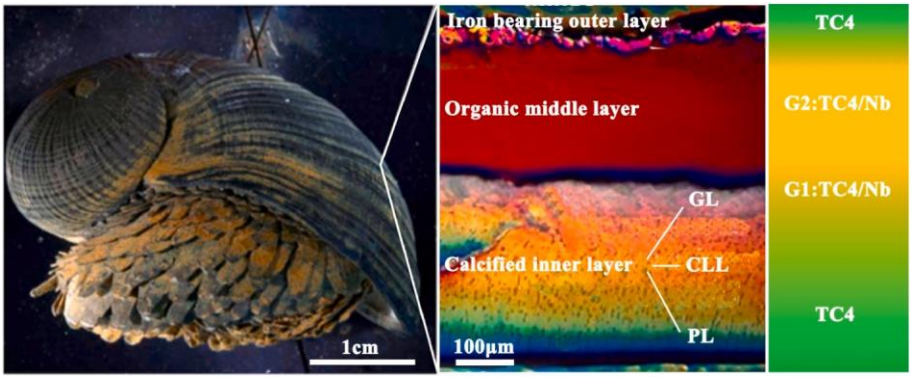

Fig. 1. The biological structure of Crysomallon squamiferum and microscopic layered structure at the cross-section of the shell [4].

Table 1
The nominal chemical compositions of the TC4 alloy and Nb wires (wt.%).

	Al	V	Fe	C	N	O	Ti	Si	Nb
TC4	6.20	4.02	0.02	0.01	0.01	0.09	Bal.	–	–
Nb	–	–	0.0014	0.001	0.002	0.005	0.001	0.005	Bal.

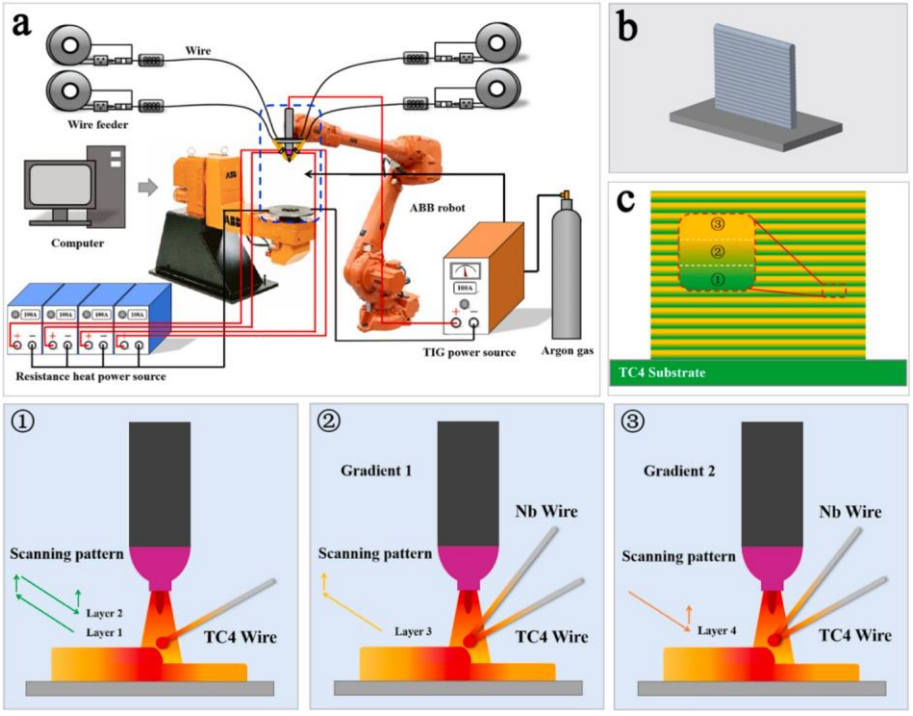

Fig. 2. (a) Schematic of the MWAAM system; (b) Diagram of the MWAAM alloy component; (c) Schematic diagram of double wire arc additive manufacturing process in different layers of MWAAM TC4/Nb multi-material alloy.

Table 2
The optimized MWAAM process parameters about this experiment.

Region	Peak current (A)	Base current (A)	TC4 wire feed velocity (cm/min)	Nb wire feed velocity (cm/min)	TC4 hot-wire current (A)	Nb hot-wire current (A)	Moving speed (mm/min)	Shielding gas flow rate (L/min)
TC4	200	9	130	–	100	–	300	20
G1	230	9	100	30	100	120	300	20
G2	230	9	70	50	100	120	300	20

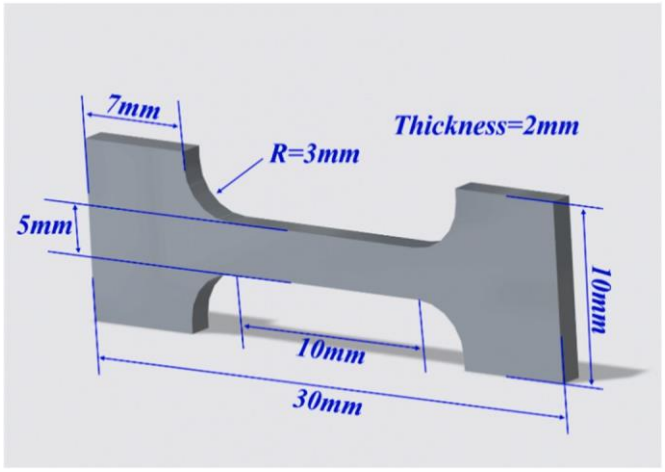

Fig. 3. Shape and dimensions (units: mm) of tensile samples.

of the common snail in terms of mechanical protection, abrasion resistance and permeability resistance. Learning the layered structure of the Crysomallon squamiferum has great potential to help develop and improve the bearing and protective engineering materials for military armor. The bionic design of layered structures has attracted wide attention [5,6]. Guo et al. [7] prepared a novel layered TiNb/NiTi superelastic composite material by a severe deformation hot pack-rolling. The results showed that the TiNb/NiTi layered structure achieved good superelasticity and biocompatibility. Yin et al. [8] studied the mode of crack propagation and fracture behavior of laminated Ti–TiNb alloy fabricated by spark plasma sintering combined with the hot rolling. They indicated that special layered structure of Ti–TiNb alloy had an enhanced strength-plasticity synergy and excellent strain hardening ability. You et al. [9] investigated the mechanical properties and electrical conductivity of heterogeneous laminated Cu/Cu–Cr–Zr composite structure prepared by accumulative roll bonding and annealing process. They found that the heterogeneity of microstructure resulted in significant hetero-deformation induced hardening, which resulted in high strength, sufficient tensile ductility and high conductivity of the structure. Ayan et al. [10] analyzed the tensile and fatigue properties of layered ER70S-6/308LSi alloy steel fabricated by wire arc additive manufacturing (WAAM) technology. The results showed that although the fabricated alloy structure contained multiple interfaces, it had strong mechanical properties in the application test. In addition, the tensile strength of this alloy component was increased by up to 46% compared to the fabrication of a single mental material. Kim et al. [11] reported that a simple process to develop heterogeneous layered alloys by wrought and laser-cladding. They indicated that the heterogeneous structure improved the yield strength and tensile strength by contributing to the strong accumulation of GNDs at the regional interface during plastic deformation compared with conventional deformation and monolithic laser cladding alloys. In addition, the layered structure increased strength with little ductility lost. The layered structures processed by these conventional processes are usually relatively complicated and limited to the shape structure and size. Therefore, it is necessary to seek a new technology to realize the fabrication of layered multi-material structure parts.

Wire arc additive manufacturing (WAAM) is one of the additive manufacturing (AM) technologies, which can be used in the manufacturing process of metal materials products and parts, especially for the additive manufacturing and remanufacturing of large metal structures or parts [12]. Compared with AM technology which uses laser or electron beam as heat source, WAAM has the advantages of fast forming rate, high forming efficiency, simple equipment, short production cycle, low cost and high material utilization rate [13,14]. With the development of WAAM technology, it has attracted great interest and wide attention all over the world, especially in the fields of aerospace aviation, weapons equipment, energy vehicles and ship manufacturing [15]. Multi-wire arc additive manufacturing (MWAAM) is a form of WAAM technology, which has been used in multi-material integrated additive manufacturing of multi-layer structures [16–18]. High performance parts can be manufactured by distributing different materials in different locations through multiple individually controllable wire feeders. Tian et al. [19] studied that the microstructure and mechanical properties of the Ni–Ti–Cr–Mo–Nb alloy prepared by dual-wire arc additive manufacturing (DWAAM). The results indicated that Ni–Ti–Cr–Mo–Nb alloy had the superelasticity at low temperature. Zhou et al. [20] reported that the microstructure evolution and tensile property of DWAAM TiAl-4822 alloy. They claimed that the prepared sample showed excellent mechanical properties under 650 °C, which resulted from the uniform of anisotropic microstructure. Bulla et al. [21] explored the effect of the local thermal cycle on microstructure

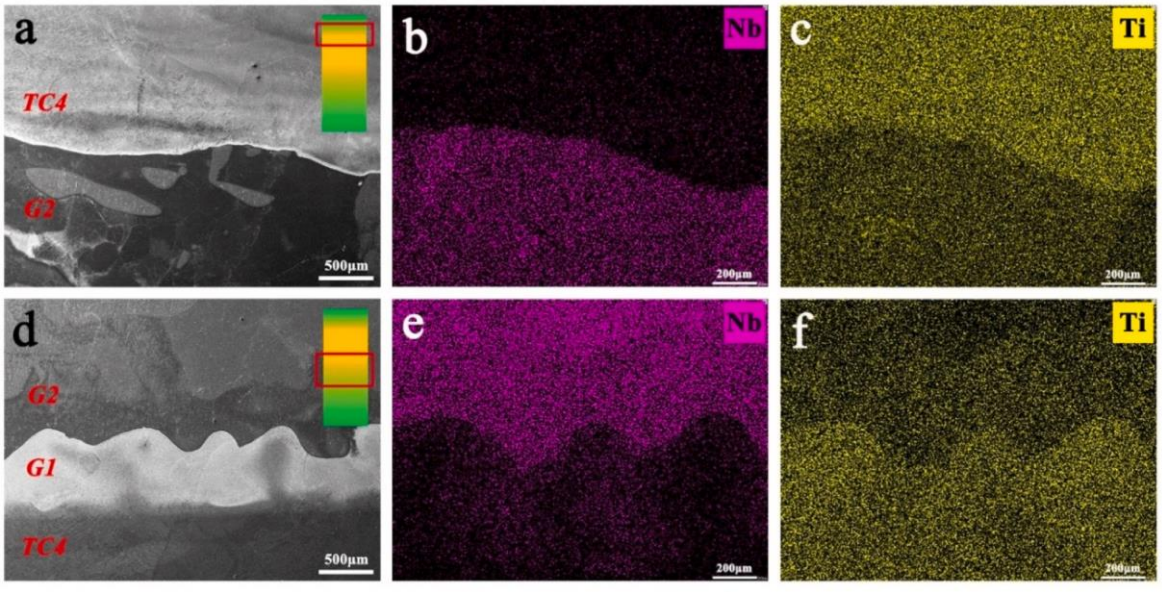

Fig. 4. The elements distribution maps around the interface of MWAAM TC4/Nb multi-material alloy: (a–c) TC4/G2 region; (d–f) G1/TC4 and G2/G1 regions.

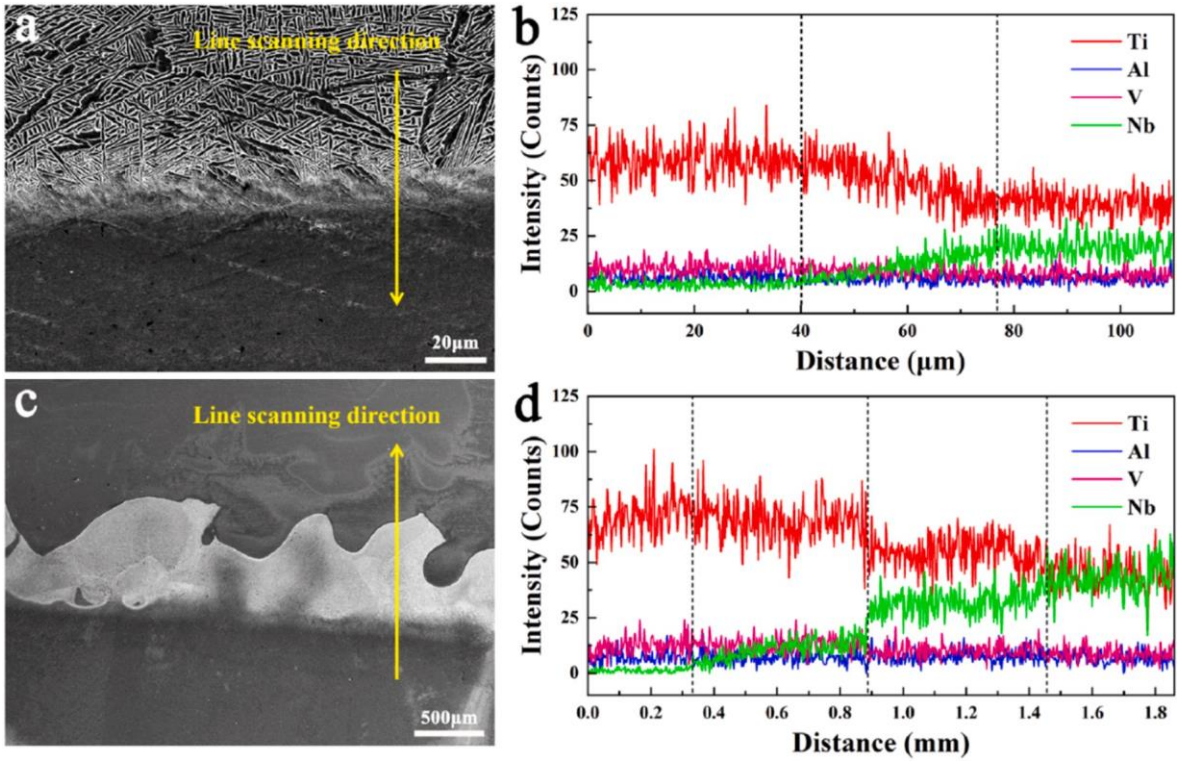

Fig. 5. EDS line scanning results along the scan paths: (a–b) TC4/G2 region; (c–d) G1/TC4 and G2/G1 regions.

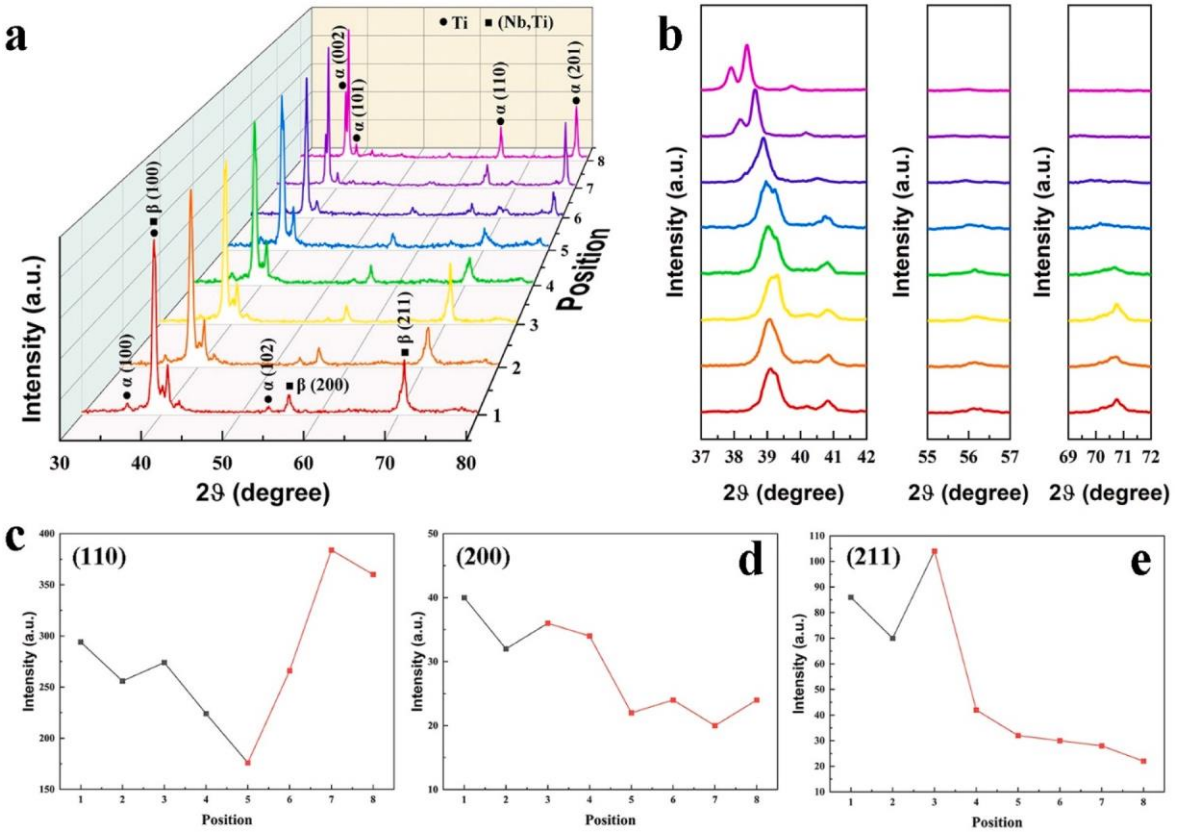

Fig. 6. (a) XRD patterns of MWAAM TC4/Nb multi-material alloy sample at different positions, (b) partial enlarged pattern of XRD, (c–e) The variation of diffraction intensity of different diffraction peaks.

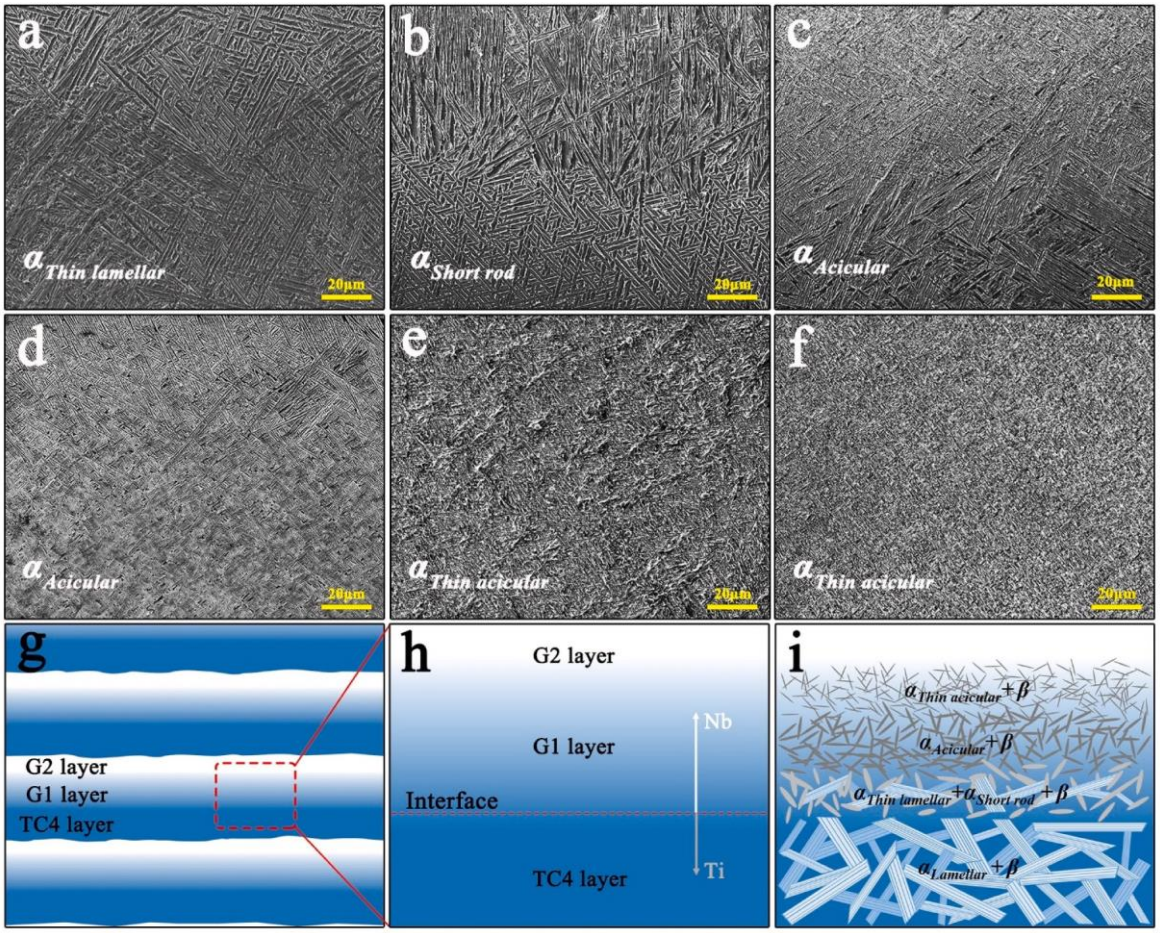

Fig. 7. (a–f) The SEM microstructure of different positions around the G1/TC4 region (from TC4 layer to G1 layer), (g–i) Schematic diagram of the formation process of the transition structure at the G1/TC4 interface.

evolution of DWAAM NiTi alloy. They showed that the chemically homogenous, fully dense NiTi alloy without defects complex phases was obtained. Meanwhile, local thermal cycling promoted the formation of Ti_5Si_3 precipitates and resulted in the formation of texture of NiTi grains.

From a brief review above, most of the multi wire arc additive manufacturing is aimed at in situ alloy manufacturing at present. There are few reports on the preparation and research of heterogeneous multi-material alloys by MWAAM. Inspired by the shell of the Crysomallon squamiferum, a heterogeneous layered by alternating hard and soft layers alloy component was designed by MWAAM. Ti6Al4V alloy (TC4) and niobium were used as the main materials for the design to manufacture bio-inspired layered multi-material parts, and the design structure is shown in Fig. 1. In this study, the bio-inspiration of this layered multi-material structure was realized by combination stiff TC4 layers and compliant TC4/Nb layers in a periodic hard-soft-hard layered form, i.e., layered TC4/Nb multi-material. Since there is no material compatibility problem between titanium alloy and Nb, unnecessary interfacial pores and cracks can be avoided by optimizing process parameters. In order to fully understand the interface reaction and functional characteristics of layered TC4/Nb heterogeneous multi-material alloy parts, the interface bonding and microstructure characteristics were discussed by analyzing the experimental results of MWAAM multi-material component. In addition, the bonding strength of the layered TC4/Nb component was evaluated by compression and tensile tests, aiming to clarify the relationship between microstructure and element distribution, i.e., the phase transformation mechanism, during the solidification as well as its impact on the mechanical of the alloy.

2. Materials and methods

2.1. Materials and experimental setup

In this work, TC4 and pure Nb (>99.95%) wires with a diameter of 1.2 mm were used as raw materials to fabricate the bionic layered heterogeneous alloy. The chemical compositions of TC4 and Nb wires are shown in Table 1. TC4 plate (150 mm × 150 mm × 5 mm) with were used as the build substrate.

The experimental setup in this work was developed by the MWAAM system, which was consisted of a 6-axis ABB robot arm with a IRC5 controller, a shielding gas unit and wire feeders. The MWAAM system is presented in Fig. 2a. The other details were introduced in our previous publication [16]. The bionic layered heterogeneous multi-material alloy component with dimensions of 80 × 8 × 60 mm^3 was fabricated on the TC4 substrate by MWAAM. The diagram of the multi-material alloy sample is shown in Fig. 2b. As shown in Fig. 2c, the multi-material alloy component consists of three parts: TC4 layer, TC4/Nb gradient 1 layer (G1) and TC4/Nb gradient 2 layer (G2). Two TC4/Nb gradient deposition layers were prepared by adjusting the ratio of TC4 and Nb wire feed speed. The three parts formed a unit and were deposited in turn to form an alloy thin wall. The schematics of the wire feeding modes and corresponding deposition paths of the three parts are shown in Fig. 2. The optimized process parameters during deposition were provided in Table 2.

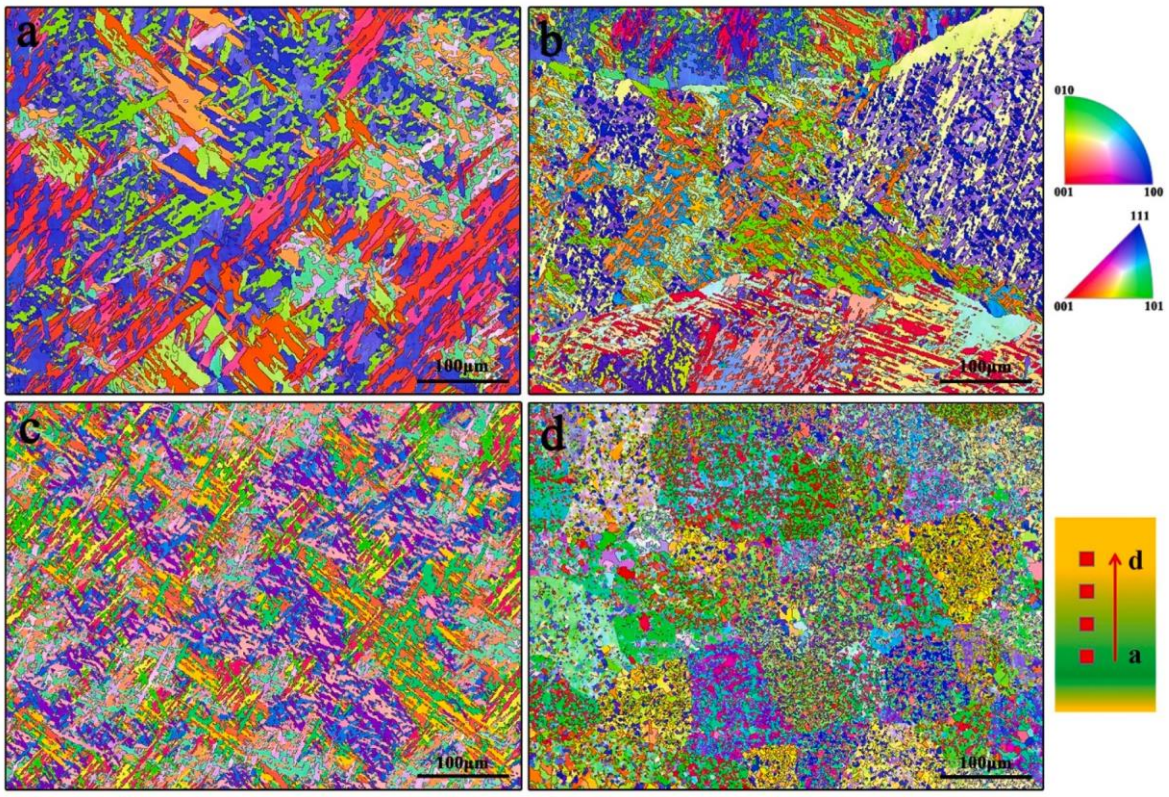

Fig. 8. EBSD orientation maps of MWAAM TC4/Nb multi-material alloy samples (from TC4 layer to G2 layer): (a) TC4 layer; (b) G1/TC4 region; (c) G1 layer; (d) G2 layer.

2.2. Microstructural characterization

The samples were separated from the TC4 substrate by wire cutting, polished with sandpaper, and then etched with a solution (1 ml HF, 6 ml HNO_3 and 100 ml H_2O) for 10 s. To identify the microstructure and elements distribution in the produced parts, the scanning electron microscopy (SEM, JSM-IT500A, Voltage: 20 kV, Average work distance: 15 mm) with the energy-dispersive X-ray spectrometer (EDS, JSM-IT500A, Voltage: 20 kV, Average work distance: 11 mm) was performed. Phase identification was performed from TC4 side to TC4/Nb side with a D/Max 2500 PC X-ray diffractometer (XRD, Voltage: 40 kV, Current: 30 mA). The diffraction angle ranged from 30° to 80° with a scanning rate of 4°/min. XRD tests were conducted at 8 consecutive locations from G2 layer to TC4 layer. Crystallographic structure and texture analysis were investigated by Electron backscatter diffraction (EBSD). EBSD data was processed by HKL Channel 5 software.

2.3. Mechanical testing

Microhardness testing was performed along the build direction with a load of 200g and a dwell time of 15s, using a Vickers automatic hardness tester (Huayin, HVS-1000). Each position was repeated three times to reduce errors. Compression tests were performed on a compression tester (Instron 1121) with a loading rate 0.5 mm/min. Three compression samples were tested to evaluated the reproducibility in terms of mechanical property. The size of compression specimens was Φ 4 mm × 8 mm. Tensile tests were performed at room temperature with an Instron 1121 machine at a displacement rate of 1 mm/min. The shape and dimensions of tensile samples are displayed in Fig. 3. Three samples for each condition (vertical and horizontal) were tested. The fracture morphologies of the failed samples were examined by SEM and EDS.

3. Results and discussion

3.1. Macro morphological characteristics and elemental distributions

In order to observe the metallurgical bonding between different deposition layers, the macro morphological and EDS scanning of different deposition interfaces were investigated. The upper interface is named as TC4/G2 region, as shown in Fig. 4a. As can be seen from Fig. 4a, TC4 layer and G2 layer formed a good metallurgical combination without defects such as cracks and pores. EDS maps of Nb and Ti elements at the interface are respectively shown in Fig. 4b-**c**. The thickness of interdiffusion zone for Nb element in TC4/G2 region was small at the interface. This phenomenon was mainly attributed to that the reduction of remelting depth. Due to the high melting temperature of Nb (2477 °C), a shallower molten pool was generated when TC4 was deposited on the G2 deposition layer, resulting in a little diffusion region of Nb elements [22]. In addition, a small number of unmelted Nb blocks can be found in G2 layer, which may be due to the unstable wire feeding speed of Nb wire during MWAAM, resulting in incomplete intermixing of TC4 and Nb metal droplets at individual locations. Similar phenomenon of unmelted particles found in the process of multi-material additive manufacturing had also reported by Wang et al. [23]. The lower region exhibited two interfaces, which are named G1/TC4 region and G2/G1 region respectively. Due to the addition of G1 layer between TC4 layer and G2 layer, the shape of the interface and the distribution of elements were changed. An interlocking interface is formed between G1 and G2 layers, as shown in Fig. 4d. As can be seen from Fig. 4e–f, G1 layer and G2 layer formed a clear interface. However, the EDS diagram of elements cannot clearly show the migration of Nb elements between TC4 layer and G1 layer, and the migration of Nb elements at G1/TC4 region will be verified in the subsequent EDS line scanning.

Fig. 5 shows the EDS line scanning results of TC4/G2 region, G1/TC4 and G2/G1 region. Since TC4 layer was deposited directly in the G2

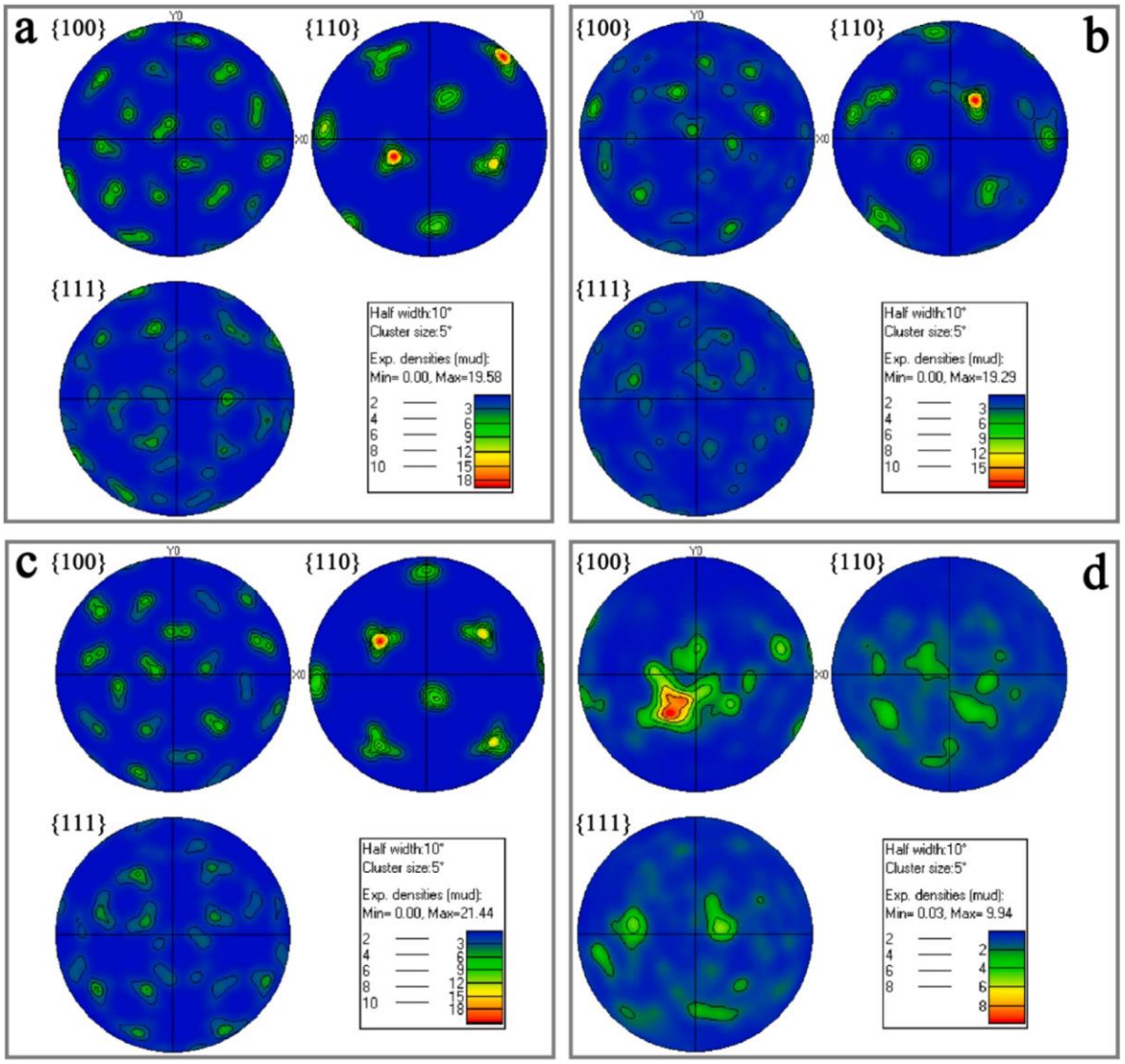

Fig. 9. Pole figures of MWAAM TC4/Nb multi-material alloy samples (from TC4 layer to G2 layer): (a) TC4 layer; (b) G1/TC4 region; (c) G1 layer; (d) G2 layer.

layer, TC4/G2 region also formed an interdiffusion zone due to remelting, and the thickness of the diffusion zone was about 36 μm, as shown in Fig. 5a–b. Compared with the interdiffusion zone of the TC4/G2 region, the interdiffusion zones of Nb and Ti elements at G1/TC4 and G2/G1 regions were larger due to the gradient design and the influence of remelting. The element migration region at G1/TC4 region and G2/G1 region were about 0.55 mm and 0.58 mm respectively, as shown in Fig. 5c–d. The further the diffusion distance of metal elements at the interface indicated the higher the metallurgical bonding strength between dissimilar metal materials [24]. Therefore, it was reasonable to conclude that the metallurgical bonding strength of G1/TC4 and G2/G1 regions was better than that of TC4/G2 region.

3.2. Phase analysis

Fig. 6a shows the phase composition of Ti/Nb multi-material alloy component in different regions. The Ti/Nb multi-material alloy component was mainly composed of α-Ti (PDF#44-1294), β-Ti (PDF#44-1288) and (Nb, Ti) solid solution (PDF#65-9436) phases, and no other intermetallic compounds had been observed. This was due to that Ti and Nb elements with higher content were completely soluble in the Ti–Nb binary phase diagram [25]. Fig. 6b is an enlarged view of the region where the characteristic peaks of the (Nb, Ti) solid solution are located. In addition, the diffraction peak intensity of crystal planes (100), (200) and (211) was statistically analyzed, as shown in Fig. 6c–e. It can be seen from Fig. 6b and 6d–e that the diffraction peak intensity of (200) and (211) of (Nb, Ti) solid solution phase was greatly weakened with the test position gradually from G2 layer to TC4 layer, which indicated that the content of (Nb, Ti) solid solution phase was gradually reduced [26]. However, the diffraction peak intensity corresponding to the crystal plane (100) decreased first and then increased, as shown in Fig. 6c. The reason for this phenomenon was that the (Nb, Ti) solid solution phase gradually transformed into β-Ti phase resulting from the increased of Ti doped in the (Nb, Ti) solid solution as the decrease of Nb content. The phenomenon that the position of the (110) diffraction peak in Fig. 6b gradually shifted to the left can also prove that the change of the content of doped Ti in the (Nb, Ti) solid solution. Similar lattice distortion of solid solutions caused by alloy atoms had been explained in detail in previous reports [27]. Since the lattice parameters of β-Ti phase and (Nb, Ti) solid solution phase was close to each other, no significant reduction in the intensity of the (110) diffraction peak was observed [28]. In addition, the intensity of α(002), α(110) and α(201) diffraction peaks gradually increased with the Ti atom content in the alloy, as shown in Fig. 6a.

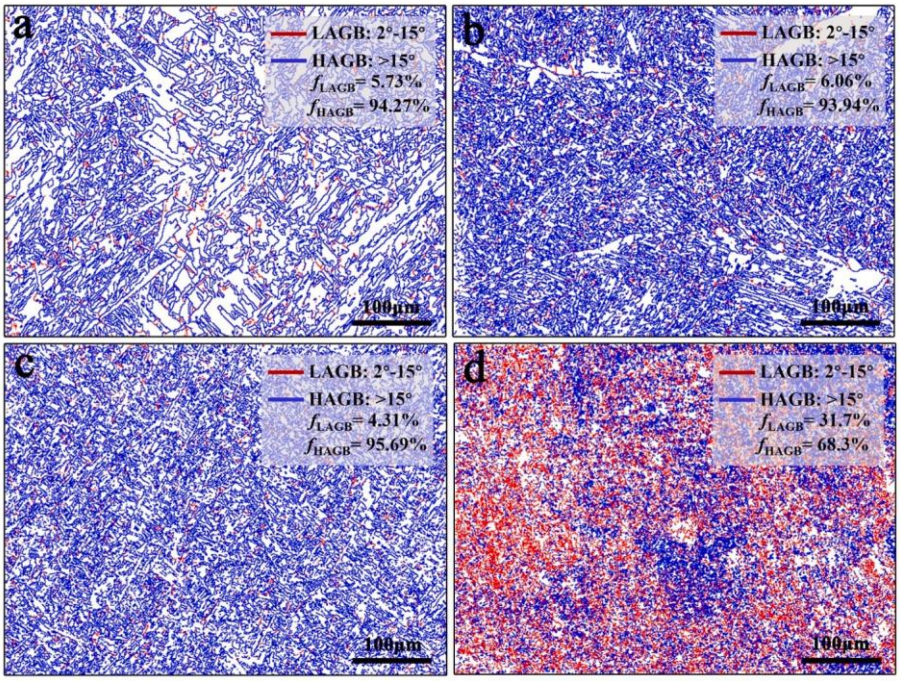

Fig. 10. Grain boundaries distribution maps of MWAAM TC4/Nb multi-material alloy samples (from TC4 layer to G2 layer): (a) TC4 layer; (b) G1/TC4 region; (c) G1 layer; (d) G2 layer.

3.3. Microstructure and crystallographic evolution

Fig. 7 shows the microstructure of different regions between the G1 layer and TC4 layer. As shown in Fig. 7a, the microstructure of TC4 layer was mainly a basketweave structure formed by the interlacing arrangement of lamellar α. As can be seen from Fig. 7a, the lamellar α was relatively large in length and width, the overall structure was typical α and β bi-phase titanium alloy structure. The microstructure of MWAAM TC4 alloy had been described in detail in previous articles [17]. Compared with Fig. 7a, the fraction of the lamellar α phase in the lower part of Fig. 7b gradually decreased, and the short rod-like α phase appeared. This difference was due to their location in different areas of the TC4 layer, which was closely related to heat dissipation conditions. When G1 layer was deposited in the top region of TC4 layer, Nb element in G1 layer would be diffused around the TC4/G1 interface region due to the remelting effect of G1 layer, and the interface with heterogeneous microstructure was formed, as shown in Fig. 7b. Meanwhile, the lamellar α phases were refined by the solution of Nb element forming a short rod and thin lamellar α phase mixed structure, as shown in the upper part of Fig. 7b. With the increase of Nb content in G1 layer, α phase size gradually decreased and β phase dominated bi-phase microstructure is formed. This was due to that Nb element was a β-phase stable element, and Nb element can form an infinite solid solution with β-Ti and finite solid solution with α-Ti when the amount of Nb in the deposit increased [29]. As the whole G1 layer contained Nb elements with a wide range, multiple microscopic structures with gradient evolution were formed in G1 layer, as shown in Fig. 7c–i. In addition, no obvious interface or boundary was found in G1 layer due to the continuous state of Nb content. The microstructure of G1 layer was mainly acicular α phase, and the lamellar α phase disappeared. Usually, the upper layer microstructure of the sedimentary layer will be coarser than the lower layer due to the thermal cycle during multilayer deposition of additive manufacturing alloy components process [30–32]. However, the α phase underwent a refinement process throughout the G1 layer, from acicular structure (Fig. 7c–d) to thin acicular structure (Fig. 7e–f). This may be due to the diffusion effect of elements in G2 layer with high Nb content, which made the top region of G1 layer contained more Nb than the bottom region of G1 layer. In addition, this phenomenon further proved that Nb element can significantly refine the α microstructure in titanium alloys. Yin et al. [29] had been reported that the morphology difference of α phase precipitation was related to the content of Nb, and the α size decreased gradually with the increase of the content of Nb. This phenomenon was consistent with the results obtained in this paper. In addition, they also found that the α phase disappeared when the content of Nb in titanium alloy reached 28 wt%. When Nb content exceeded 40 wt%, metastable β phase can be retained from high temperature by rapid cooling. Since the content of Nb in G1 layer did not reach wt.%, thin acicular α phase was also observed at the top of G1 layer, as shown in Fig. 7f.

The microstructure evolution schematic diagram between TC4 layer and G1 layer is shown in Fig. 7g–i. With the increase of Nb content, the morphology of phase underwent a continuous transformation process from TC4 layer to G1 layer: Lamellar α + β →Thin lamellar α + Short rod α ß → Acicular α ß→ Thin acicular α ß. The results showed that α phase with specific size and morphology can be obtained by changing the content of Nb in the bi-phase titanium alloy. The composition of G2 layer was relatively stable and the microstructure of G2 layer was relatively simple, as shown in Fig. 5. Therefore, the relevant discussions will be described later.

In order to study the crystallographic characteristics of TC4/Nb multi-material components, four regions were selected from TC4 layer to G2 layer for analysis. The EBSD orientation maps of different regions is shown in Fig. 8. The grain orientation diagram showed the orientation relationship between different grains with different colors and different orientation. Red represented the <001> direction, blue represented the <111> direction, and green represented the <101> direction. As can be seen from Fig. 8a, most of the TC4 layers were lamellar α phases. Many adjacent and parallel layers fused together to form a larger region, that was the colony α structure. It was a relatively large phase in the grain orientation diagram, and the size of these colony α had a very important effect on the mechanical properties of the alloy component [33]. In some regions, the lamellar α phase grew with a certain orientation, which formed the basketweave structure. The phase evolution in the titanium alloy component deposited by the WAAM follows the Burgers

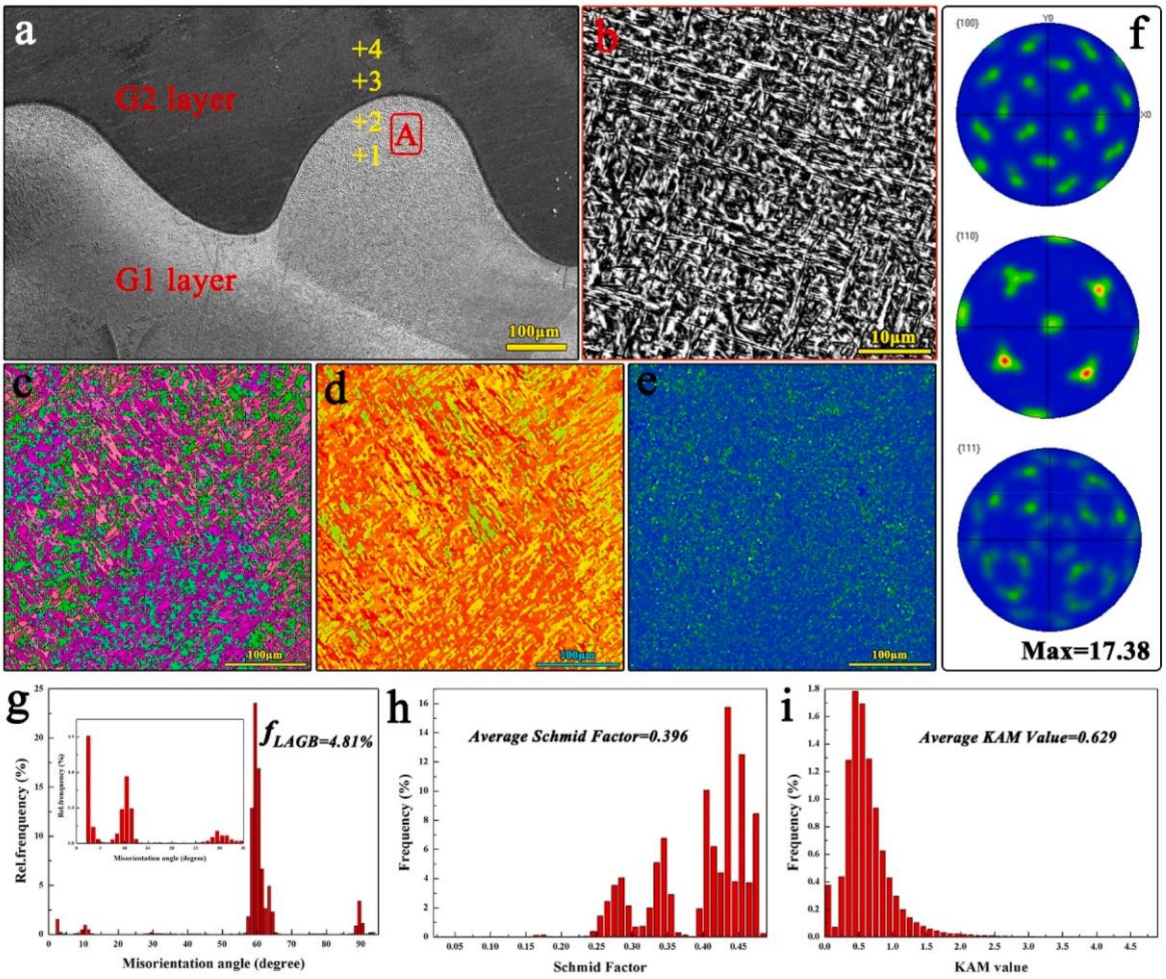

Fig. 11. SEM and EBSD results of G2/G1 region of MWAAM TC4/Nb multi-material alloy: (a–b) SEM images; (c) Grain morphology; (d) Schmidt factor distribution map; (e) KAM value distribution map; (f) Pole figure; (g) Statistics charts of misorientation angle; (h) Statistics charts of Schmidt factor; (i) Statistics charts of KAM value.

Table 3
EDS results of selected points in Fig. 11a (wt.%).

Position	Ti	Nb	Al	V
1	77.09	14.50	4.95	3.46
2	72.15	21.51	3.74	2.60
3	62.79	31.75	3.52	1.94
4	59.13	34.97	3.30	2.60

orientation relationship [16], i.e. $(0001)_{\alpha}//(110)_{\beta}$. Based on Burgers orientation relationship, it can be known that an individual body centered cubic crystal can be transformed into 12 hexagonal close packed crystals with different orientation from the original β crystal, that is, any one of the six (110) slip planes can be transformed into a (0001) crystallographic plane. Meanwhile, there are two different slip directions for the (0001) crystallographic plane. Therefore, it was possible to repeat the orientation of the layered α many times due to the large number of orientations during crystal transition, thus forming a net-like structure similar to a net basket. The selected location was near the TC4/G1 interface region, and the width of the lamellar α phase decreased obviously, as shown in Fig. 8b. In addition, the large colony α phase was also found in this region. Most of the grains in the G1 layer were acicular, as shown in Fig. 8c. Fig. 8d shows the grain orientation distribution of G2 layer. Compared with TC4 and G1 layers, the grain shape of G2 layer changed significantly, and most of the grains were fragmentary. This was due to that the content of Nb was high in G2 layer, where a large number of (Nb, Ti) solid solution phases were formed. Since the Nb content showed a gradual upward trend, the statistics of grain size, texture evolution, and misorientation angle distribution were conducted to study the influence of Nb content on crystallographic evolution in TC4/Nb multi-material alloy component. The average grain sizes of the four regions were 3.534 μm, 3.228 μm, 2.975 μm and 2.904 μm, respectively. The results showed that the grain size of TC4/Nb multi material alloy component from TC4 layer to G2 layer gradually decreased with the increase of Nb content, which further proved that Nb element can refine the titanium alloy structure.

As we all known, when the grain orientations of polycrystalline metal materials were concentrated near one or some orientations, the preferred orientations will be formed, and then the texture will be formed in the polycrystal [34]. In order to analyze the texture strength, the polar density of different regions was obtained by EBSD. The polar diagram of the four regions is shown in Fig. 9. As can be seen from Fig. 9a–c, the three regions between TC4 layer and G1 layer showed the strong {110}, texture, and the corresponding pole densities are 19.58, 19.29, and 21.44, respectively. However, the region of G2 layer showed relatively weak {100} texture, with a maximum intensity of 9.94, as show in Fig. 9d. In addition, the distribution of texture intensity of G2 layer was found to varied greatly, which indicated that G2 layer had a tendency to shift from fibrous to recrystallized texture [35].

Fig. 10 shows the grain boundaries distribution map of TC4/Nb

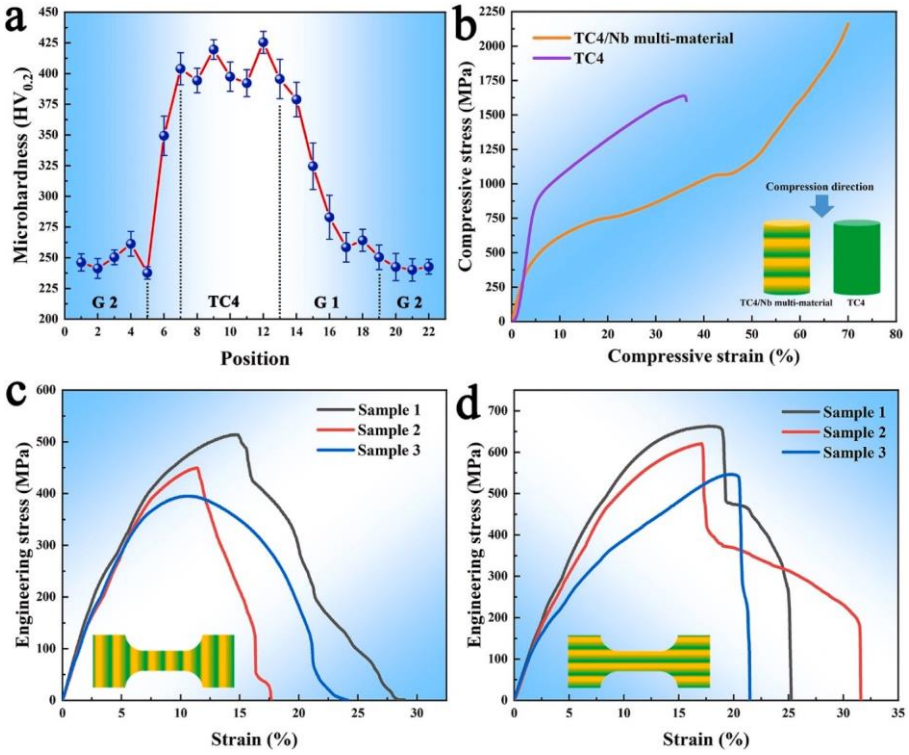

Fig. 12. Mechanical test of MWAAM TC4/Nb multi-material alloy: (a) Vickers hardness values distribution; (b) Compression stress-strain curves; (c) Longitudinal direction tensile stress-strain curves; (d) Transverse direction tensile stress-strain curves.

Table 4
Compression properties (room temperature) of WMAAM specimens.

Specimen	$\sigma_{0.2}$ (MPa)	σ_{max} (MPa)
TC4	872.24 ± 15	1638.54 ± 16
TC4/Nb multi-material	478.14 ± 22	2162.64 ± 26

Table 5
Tensile properties (room temperature) of WMAAM specimens.

	Specimen	UTS(MPa)	EL(%)
Longitudinal direction	1	514.21	14.59
	2	449.54	11.40
	3	395.12	10.97
Transverse direction	1	663.39	17.77
	2	620.99	17.08
	3	546.62	19.92

multi-material alloy sample. The grain boundaries can be classified as high angle grain boundaries (HAGBs, $\theta > 15°$) and low angle grain boundaries (LAGBs, $2° < \theta < 15°$) according to the orientation angle θ between adjacent grain orientation [36]. The grain boundary ratio of the corresponding grain boundaries distribution map is obtained through calculation (the top right portion of Fig. 10). The proportion of LAGBs in the three regions between TC4 layer and G1 layer changed little (5.73%, 6.06% and 4.31%, respectively), while the proportion of LAGBs in G2 region increased significantly to 31.7%. The fine microstructure of metal materials during solidification indicated that more dislocations were formed in the alloy [36]. When the dislocation density reached a certain critical value, dislocation dynamic recovery took place through annihilation and rearrangement to reduce the storage energy and then dislocation cells formed [37]. The dislocation cells transformed into sub-grains with LAGBs with further deformation. Therefore, G2 layer had a higher proportion of LAGBs. In addition, high density dislocation can also generate a large number of substructures within the grain, which in turn impeded the movement of the dislocation and resulted in an increase in the strength of the material [38]. The grain boundary energy γ_{gb} can be calculated by the Read-Shockley equation based on dislocation theory [39]:

$$\gamma_{gb} = \gamma_0\theta(1\text{-}\ln\theta/\theta_m) \quad (1)$$

$$\gamma_0 = Gb/4\pi(1\text{-}v) \quad (2)$$

where θ and θ_m represented grain boundary angle and the angle at which the grain boundary energy reached its maximum value of γ_{gb}, respectively. G was Shear modulus, b was Burgers vector and v was Poisson ratio. According to equations (1) and (2), the grain boundary energy γ_{gb} of LAGBs was lower than that of HAGBs. This showed that HAGBs can more effectively hinder dislocation motion and inhibit or even prevent crack propagation than LAGBs, so as to improve the toughness and other properties of the alloy.

In particular, the microstructure and element distribution at the interface of G2/G1 region were analyzed. Fig. 11a shows the microstructure of G2/G1 region. It can be seen from Fig. 11a that a cross-like interface was formed between G2 layer and G1 layer. EDS element distribution at the interface was tested, and the results are shown in Table 3. The results showed that the content of Nb element increased gradually from G1 layer to G2 layer, indicating that the interdiffusion behavior of elements also formed at the interface. However, G2 layer was mainly composed of (Nb,Ti) solid solution phase and contained a high amount of Nb (more than 30 wt%), and no special microstructure can be observed. Therefore, only the near-G1 side region A around the G2/G1 interface was analyzed in detail. Fig. 11b is an enlarged view of a local region A of Fig. 11a. The microstructure of the region A was 90° crossed fine acicular. Fig. 11c–e shows grain orientation distribution, Schmidt factor distribution and kernel average misorientation maps of region A respectively, and the corresponding histogram is shown in Fig. 11g–i. The results showed that the crystal had a certain preferred orientation in region A. Through the pole density analysis of the texture,

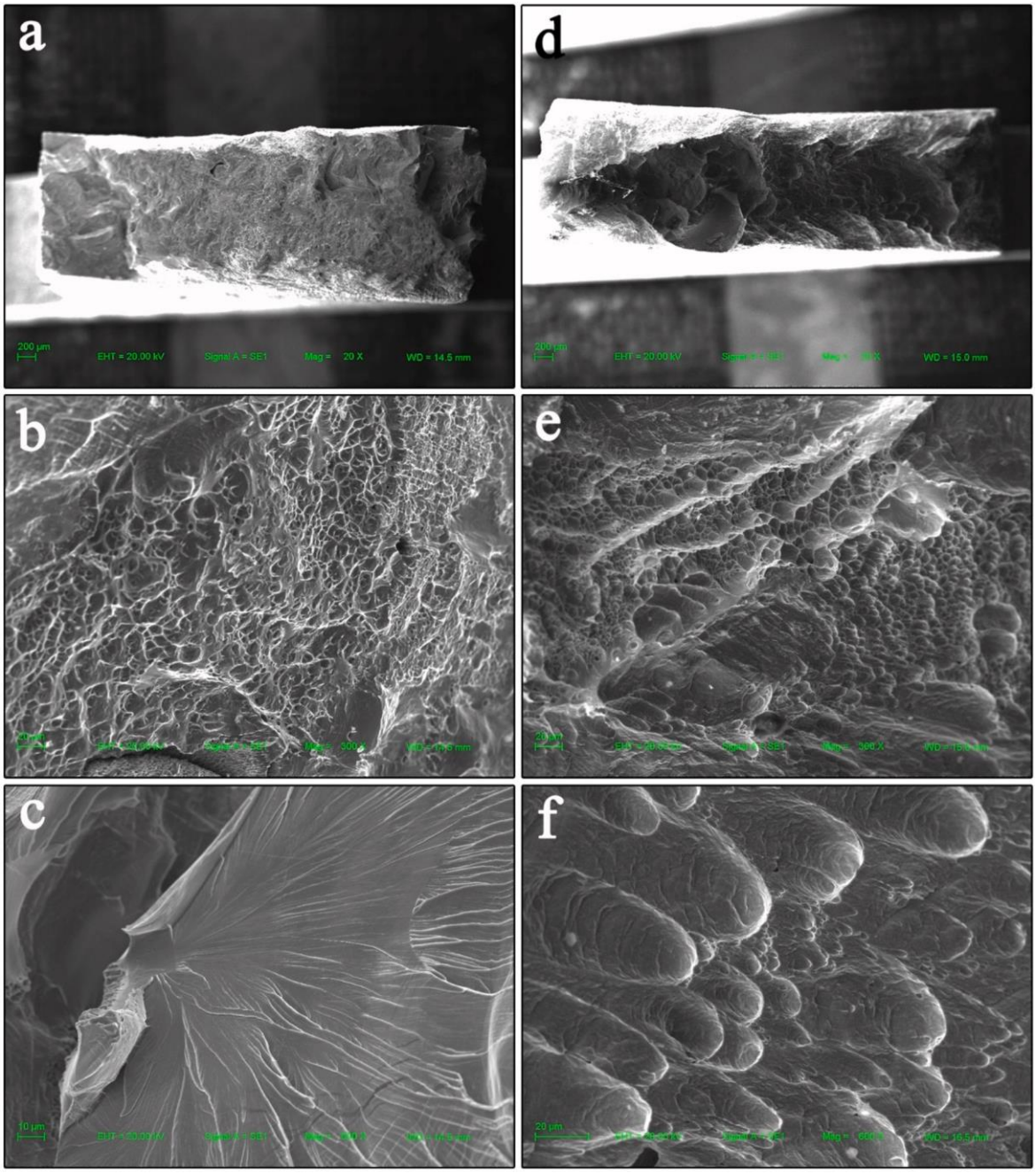

Fig. 13. The fracture surfaces of MWAAM TC4/Nb multi-material alloy: (a, d) low-magnification SEM images; (b-c, e-f) The high-magnification SEM images. (a–c) Longitudinal direction tensile samples; (d–f) Transverse direction tensile samples.

it was known that a (110) texture with an intensity of 17.38 had been formed, as shown in Fig. 11f. This was due to that single reciprocating scanning mode played a role in strengthening anisotropy during the MWAAM TC4/Nb multi material alloy component process. The region A was dominated by LAGBs, and its proportion was 95.18%, as shown in Fig. 11g. Meanwhile, the average Schmidt factor value and the average KAM value were calculated by statistical analysis of the Schmidt factor and kernel average misorientation as 0.396 and 0.629 respectively, as shown in Fig. 11h–i. In the process of metal deformation, the sliding system with large Schmidt factor was preferentially activated. As can be seen from Fig. 11d, the distribution of Schmidt factor was relatively uniform, indicating that there was little difference in the performance of region A in all directions. Dislocation density also had an important effect on the strength and toughness of materials. The geometrically necessary dislocation (GND) density in region A can be calculated as follows [37]:

$$\rho_{GND} = 2\varphi/\mu b \tag{3}$$

where φ was average misorientation value, μ was the 1 μm scan step, and b was 0.255 nm Burgers vector [40]. According to equation (3), the geometrically necessary dislocation density of region A can be obtained, which was 4.933×10^{15} m^{-2}.

3.4. Mechanical properties

3.4.1. Microhardness

In order to study the microhardness distribution of TC4/Nb multi-material metal parts prepared by MWAAM, microhardness

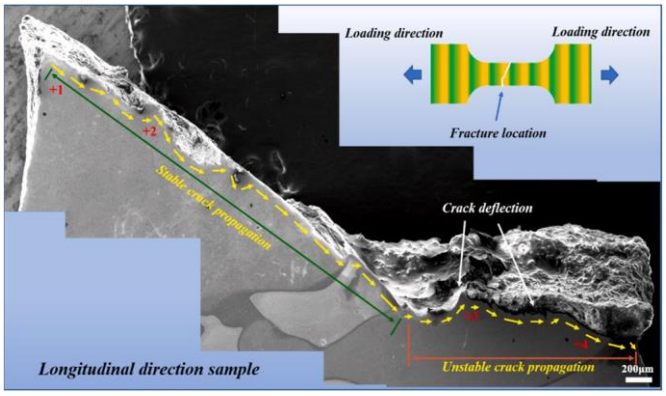

Fig. 14. SEM images of the crack propagation path of MWAAM TC4/Nb multi-material alloy in longitudinal direction.

Table 6
EDS results of selected points in Fig. 14 (wt.%).

Position	Ti	Nb	Al	V
1	55.75	37.79	4.14	2.32
2	56.05	38.32	3.49	2.14
3	66.86	25.56	4.06	3.52
4	87.05	4.34	4.60	4.01

measurement across layered structures along the building direction were carried out, as shown in Fig. 12a. The results showed that the microhardness changed significantly in three different regions corresponding to TC4/G1/G2 layers. The average microhardness of TC4 layer was 404.04 HV, and the peak value was 425.35 HV. The microhardness of G1 layer gradually decreased from 378.87 HV to 250.35 HV under the action of gradient interfacial diffusion and interfacial reaction products until it reached G2 layer. The microhardness distribution of G2 layer fluctuated little, and the average microhardness was 245.23 HV. In conclusion, the microhardness of TC4→G1→G2 layer decreased gradually in the building direction of layered multi-material. The existence of gradient zone helped to form a good metallurgical bond between different materials. Gu et al. [23] had reported that smooth hardness transition and atomic migration at the interface were conducive to release of residual stress and improve comprehensive mechanical properties. In addition, the gradient zone acts as a buffer between the hard and soft materials. Due to the different elastic modulus and thermal expansion coefficient of different materials in the multi-material structural parts, when a material was subjected to external force or temperature changed in work, the multi-material integral component will produce different degrees of deformation [41]. As a result, the bonding interface of multiple materials created a huge concentration of stress. When the stress exceeded the bonding strength, the crack will start and spread. Therefore, the gradient zone can effectively reduce the sensitivity of cracking between different materials of multi-material structural parts.

3.4.2. Compression behavior

In this work, the compression test of the MWAAM TC4/Nb multi-material alloy was terminated while the strain reached 70%. The compression curves of MWAAM TC4 and MWAAM TC4/Nb multi-material alloy as shown in Fig. 12b. The curves of the two alloys were quite different, and the related compression strength of two alloy samples were obtained in Table 4. The $\sigma_{0.2}$ of TC4/Nb multi-material alloy and TC4 samples were 478.14 ± 22 MPa and 872.24 ± 15 MPa, respectively. The 0.2% offset compression strength ($\sigma_{0.2}$) of TC4 sample was higher than TC4/Nb multi-material alloy sample. While the value of maximum compression strength (σ_{max}) was different, the σ_{max} of TC4/Nb multi-material alloy sample was 2162.64± 26 MPa, which was 31.99% higher than that of the TC4 sample (1638.54± 16 MPa). Overall, the compressive strength of TC4/Nb multi-material structure was greatly improved by materials combination and bionic design.

3.4.3. Tensile behavior

The stress-strain curves of the three tensile test specimens in the longitudinal and transverse directions were shown in Fig. 12c–d. Each group contains ultimate tensile strength (UTS) and elongation rate (EL), the values of UTS and EL of MWAAM TC4/Nb multi-material alloy samples were summarized in Table 5. The results showed that the samples differed greatly in two directions of UTS. The average UTS of longitudinal direction was 452.96 MPa and the maximum UTS was 514.21 MPa, corresponding to the EL of 14.59%. However, the tensile strength and elongation of the transverse direction samples were higher than that of the longitudinal direction samples. The average UTS of transverse direction was 610.33 MPa and the maximum UTS was 663.39 MPa, corresponding to the EL of 17.77%. In addition, as can be seen from Fig. 12d, fracture instability occurred in the transverse direction sample before complete fracture. This was because the multi-layer material structure presented a hard-soft-hard distribution, and the first fracture failure tended to occur on the softer side of the material, resulting in the change of fracture mode from stretching to in-plane shear during the tensile process [42]. This phenomenon will reduce the toughness of the material. Similar phenomenon had been observed by Wu et al. [43] in the tensile test of wire arc additive manufacturing steel-nickel bimetallic component.

In order to systematically reveal the fracture mechanism of tensile specimens, the fracture morphology was analyzed by scanning electron microscopy. Fig. 13 shows the fracture morphologies of MWAAM TC4/Nb multi-material alloy samples in different directions. As can be seen from Fig. 13a, the macro fracture morphology of longitudinal tensile sample mainly presented a tear shape, and the two ends of the fracture showed a step shape. It was difficult to distinguish the fiber region, the radical region and the shear lip, and the corresponding characteristics were difficult to distinguish. In addition, the necking phenomenon of longitudinal tensile specimens was not obvious. As can be seen in Fig. 13b, the steps were covered with shallow dimples of varying sizes. There were also small steps formed by a small number of quasi-cleavage facets and river pattern features, as indicated in Fig. 13c. Therefore, the fracture mode of the longitudinal tensile samples was a mixture of ductile fracture and brittle fracture. Fig. 13d–f shows the fracture morphology of transverse tensile samples. As can be seen from Fig. 13d, the middle area of the fracture was significantly lower than the shear lip area of the fracture edge, and the fracture had an obvious necking phenomenon. There were many dimples of different sizes distributed in the fracture, as shown in Fig. 13d. In addition, the small dimple zone distributed around the tear edge of different shapes, as shown in Fig. 13e. The dimples in the dimple zone were small and dense. Moreover, most dimple shapes were not equiaxial, but parabolic, as shown in Fig. 13e. This was due to the fact that the dimples were elongated along a certain direction during the tearing process resulting from the heterogeneity of the multi-material alloy samples. Such dimples characteristics was the reason inducing the transverse tensile strength was higher than the longitudinal strength of the MWAAM TC4/Nb multi-material alloy samples. In addition, a large number of protruding columns formed on the other side of the fracture, further supporting the existence of a large number of dimples, as shown in Fig. 13f. Therefore, the fracture mode of transverse tensile specimens was mainly ductile fracture.

The structure morphology and interlayer bonding strength of multilayer materials will produce different levels of mechanical properties. The toughness of different materials is different, which leads to different crack propagation behavior. In order to better explore the crack growth mechanism, the macroscopic crack growth path of a representative longitudinal tensile sample fracture was studied in

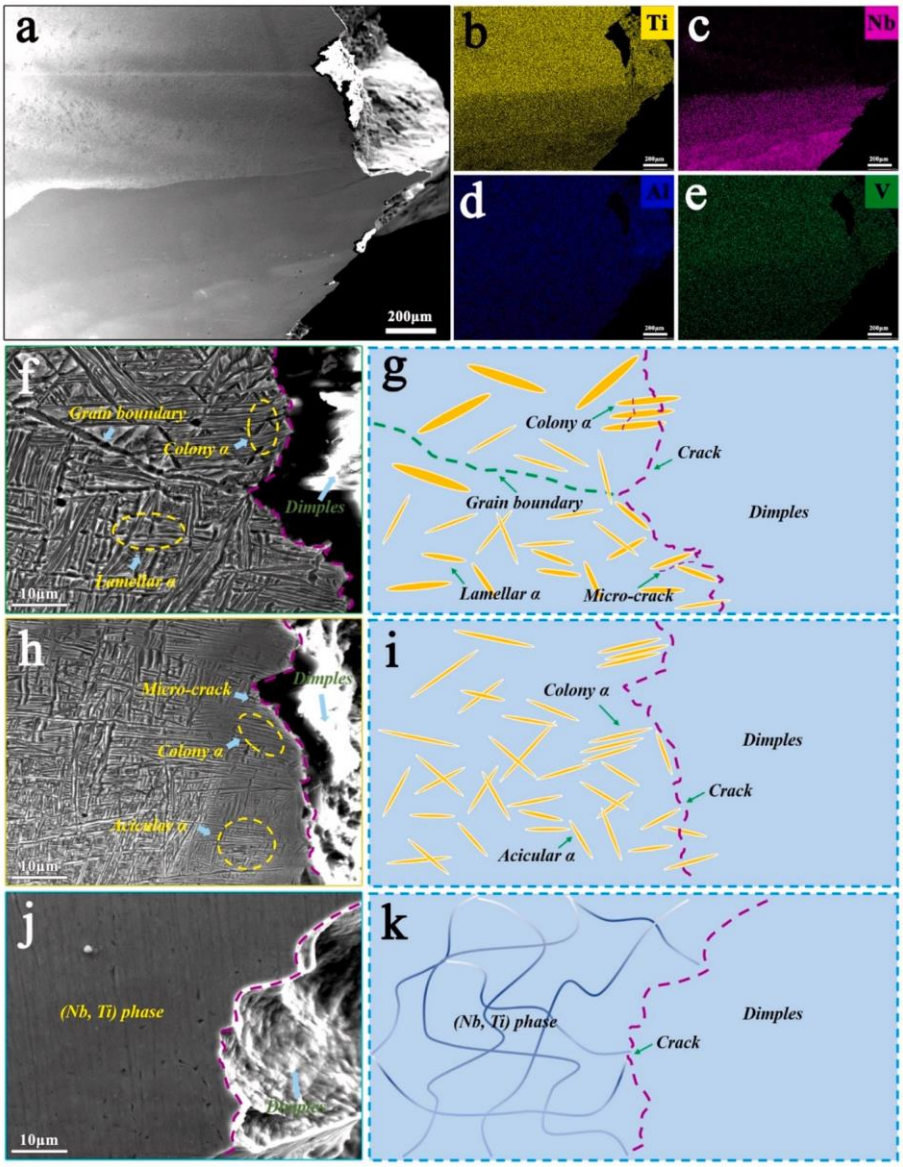

Fig. 15. (a–e) SEM images and EDS maps of the crack propagation path of MWAAM TC4/Nb multi-material alloy in transverse direction. The crack propagation path in different layers and corresponding schematic diagrams: (f–g) TC4 layer; (h–i) G1 layer; (j–k) G2 layer.

Fig. 14. It was well known that crack growth can be divided into two parts: stable crack propagation stage and unstable crack propagation stage. It can be seen from Fig. 14 that the crack growth path was relatively smooth in the stable propagation stage. In the unstable propagation stage, the deflection angle of crack growth path changed greatly. Liu et al. [44] also reported a similar phenomenon. And they found that the more ductile the metal, the more tortuous the crack propagation path. In addition, EDS measurements were performed around the fracture to determine the location of the fracture crack in the TC4/Nb multi-material component, the results as shown in Table 6. EDS results showed that the fracture originated in TC4/G2 region and ended in G1 region. This was due to that the grain boundary density was higher in the G2 region, where dislocation was prone to stress concentration, as shown in Fig. 10d. In addition, the LAGBs in G2 region accounted for a large proportion, and the dislocation energy consumption was small in the process of dislocation movement. Therefore, the crack growth in G2 region was smooth, forming a crack stable growth region, as show in Fig. 14. However, the Schmidt factor distribution in G1 region was relatively uniform and the stress was small, as shown in Fig. 11d–e, so the crack propagation path in G1 region was tortuous. Therefore, it was reasonable to conclude that among the three interfaces of TC4/Nb multi-material components, the bonding strength of G1/TC4 region at the interface was better than that of G2/G1 region at the interface, and the bonding strength of TC4/G2 region at the interface was relatively worst.

Fig. 15 shows EDS maps and crack growth path and corresponding schematic diagram of the fracture of representative sample in transverse direction. Fig. 15a shows the SEM image of crack propagation shape in TC4/Nb multi-material alloy component. Combined with the distribution of elements in Fig. 15b–e, the distribution of TC4 layer, G1 layer and G2 layer can be clearly distinguished. It can be observed that α phases were torn in the process of crack growth by locally enlarging SEM of the TC4 layer, which showed obvious transgranular fracture characteristics, as shown in Fig. 15f–g. In addition, microcracks including secondary cracks were observed in TC4 layer, which can consume a lot of energy during crack propagation and significantly improve fracture toughness.

Fig. 15h–i shows the SEM of G1 layer and the corresponding schematic diagram, from which it can be seen that the crack mainly propagated at the edge of acicular colony α. This can be attributed to that the dense acicular α intensified the stress concentration phenomenon in G1

layer and was easy to form dislocation plugs, which provided favorable conditions for the formation of voids and accelerated the propagation of cracks. Therefore, the crack growth path in Fig. 15h was relatively flat. Fig. 15j–k shows the SEM of the G2 layer and the corresponding schematic diagram. The G2 layer was mainly composed of (Nb, Ti) solid solution phase due to the high Nb content, the typical α and β bi-phase microstructure was not observed. In addition, from the results of the previous microhardness distribution test (Fig. 12a), it can be seen that the hardness of G2 layer was relatively low, so the crack propagates quickly in G2 layer, and the fracture morphology was smooth, as shown in Fig. 15j.

4. Conclusions

In this study, a TC4/Nb multi-material structure inspired by the shell of Crysomallon squamiferum was designed and manufactured by MWAAM, and it exhibited excellent mechanical properties. The interfacial reaction, phase composition, microstructure evolution, crystal growth, mechanical properties and crack propagation of MWAAM-processed bionic heterogeneous TC4/Nb multi-material alloy component were studied. The main results are summarized as follows.

(1) Based on the analyzed the results of element interdiffusion behavior of the G1/TC4, G2/G1 and TC4/G2 interface regions, it can be found that good metallurgical combination was obtained between different layers. The Ti/Nb multi-material alloy component was mainly composed of α-Ti, β-Ti and (Nb, Ti) solid solution phases, and no other intermetallic compounds formed. The β-Ti phase gradually transformed into (Nb, Ti) solid solution phase resulting from the increased of Nb doped in the β-Ti phase as the increase of Nb content.

(2) The morphology of phase underwent a continuous transformation process from TC4 layer to G1 layer with the increase of Nb content: Lamellar α + β →Thin lamellar α + Short rod α + β → Acicular α + β → Thin acicular α + β. The grain size of TC4/Nb multi material alloy component from TC4 layer to G2 layer gradually from 3.534 μm decreased to 2.904 μm with the increase of Nb content. In addition, the texture intensity and the proportion of HAGBs of G2 layer were decreased due to the formation of a large number of (Nb, Ti) solid solutions in the G2 layer.

(3) The microhardness of TC4/Nb multi-material alloy from TC4 layer to G2 layer ranged from 404.04 HV to 245.23 HV. The maximum compression strength of TC4/Nb multi-material alloy sample was 2162.64 ±26 MPa, which was 31.99% higher than that of the TC4 sample (1638.54 ±16 MPa). The maximum UTS of longitudinal direction and transverse direction tensile samples were 514.21 MPa and 663.39 MPa, and the maximum EL of longitudinal direction and transverse direction were 14.59% and 17.77%, respectively.

(4) The fracture mode of longitudinal tensile sample was a mixture of ductile fracture and brittle fracture, while the fracture mode of transverse tensile sample was mainly ductile fracture. Crack propagation was mainly dominated by crack deflection and multistage cracking. The bonding strength of G1/TC4 region at the interface was better than that of G2/G1 and TC4/G2 regions at the interface. It is found that the crack propagation path of TC4 layer was the most tortuous in the fracture observation of the transverse tensile sample, indicating that the strength of TC4 layer was the highest than G1 and G2 layer in the TC4/Nb multi-material alloy component.

CRediT authorship contribution statement

P.F. Jiang: Writing – original draft, Formal analysis, Data curation. **M.H. Nie:** Data curation. **J.Z. Teng:** Investigation. **X.B. Wang:** Resources. **C.Z. Liu:** Formal analysis. **Z.H. Zhang:** Validation.

Declaration of competing interest

The authors declare that they have no known competing financial interests or personal relationships that could have appeared to influence the work reported in this paper.

Data availability

No data was used for the research described in the article.

Acknowledgements

This work is supported by the National Key Research and Development Program of China (Grant 2022YFB4600500) and the National Natural Science Foundation of China (Grant 52235006 and 52025053).

References

[1] N. Aage, E. Andreassen, B.S. Lazarov, O. Sigmund, Giga-voxel computational morphogenesis for structural design, Nature 550 (2017) 84–86.
[2] A. Velasco-Hogan, J. Xu, M.A. Meyers, Additive manufacturing as a method to design and optimize bioinspired structures, Adv. Mater. 30 (2018), 1800940.
[3] A. Nojoomi, H. Arslan, K. Lee, K. Yum, Bioinspired 3D structures with programmable morphologies and motions, Nat. Commun. 9 (2018) 3705.
[4] H.M. Yao, M. Dao, T. Imholt, J.M. Huang, K. Wheeler, A. Bonilla, S. Suresh, C. Ortiz, Protection mechanisms of the iron-plated armor of a deep-sea hydrothermal vent gastropod, P. Natl. Acad. Sci. Unit. States Am. 107 (2010)987–992.
[5] W. Yanfeng, L. Zhengxian, W. Haonan, D. Jihong, Z. Changwei, Effect of multilayered structure on properties of Ti/TiN coating, Rare Met. Mater. Eng. 46 (2017) 1219–1224.
[6] H. Zhu, W. Sun, F. Kong, X. Wang, Z. Song, Y. Chen, Interfacial characteristics and mechanical properties of TiAl/Ti6Al4V laminate composite (LMC) fabricated by vacuum hot pressing, Mater. Sci. Eng., A 742 (2019) 704–711.
[7] S. Guo, Y.L. Shi, R.T. Wu, H.X. Liu, Q.K. Meng, G.L. Liu, X.N. Cheng, X.Q. Zhao, Deformation behavior of a novel sandwich-like TiNb/NiTi composite with good biocompatibility and superelasticity, Mater. Sci. Eng., A 794 (2020), 139784.
[8] Y.F. Yin, W.J. Kou, Y.Q. Zhao, X. Li, B.J. Zhang, W.D. Zeng, Deformation behavior and fracture mechanism of laminated Ti/Ti-50 Nb alloy with diffusion layer, J. Alloys Compd. 933 (2023), 197754.
[9] C. You, L. Zeng, R. Gao, X. Zhang, H. Wang, A dual heterogeneous laminated microstructure design for improving the mechanical properties and electrical conductivity of copper alloys, Mater. Char. 187 (2022), 111878.
[10] Y. Ayan, N. Kahraman, Fabrication and characterization of functionally graded material (FGM) structure containing two dissimilar steels (ER70S-6 and 308LSi) by wire arc additive manufacturing (WAAM), Mater. Today Commun. 33 (2022), 104457.
[11] R.E. Kim, E.S. Kim, G.M. Karthik, G.H. Gu, S.Y. Ahn, H. Park, J. Moon, H.S. Kim, Heterostructured alloys with enhanced strength-ductility synergy through laser-cladding, Scripta Mater. 215 (2022), 114732.
[12] C. Xue, Y. Zhang, P. Mao, C. Liu, Y. Guo, F. Qian, C. Zhang, K. Liu, M. Zhang, S. Tang, et al., Improving mechanical properties of wire arc additively manufactured AA2196 Al–Li alloy by controlling solidification defects, Addit. Manuf. 43 (2021), 102019.
[13] Y.B. Tian, X.Y. Chen, Y.C. Cai, Z. Luo, M.F. Chen, X. Zhang, J.G. Li, J. Han, Microstructure and properties of a Ni–Ti–Cr–Mo–Nb alloy fabricated in situ by dual-wire arc additive manufacturing, Mater. Sci. Eng., A 15 (2022), 143740.
[14] J. Han, G.Y. Zhang, X.Y. Chen, Y.C. Cai, Z. Luo, X. Zhang, Y. Su, Y.B. Tian, High strength Ti alloy fabricated by directed energy deposition with in-situ Cu alloying, J. Mater. Process. Technol. 310 (2022), 117759.
[15] C.R. Cunningham, J.M. Flynn, A. Shokrani, V. Dhokia, S.T. Newman, Invited review article: strategies and processes for high quality wire arc additive manufacturing, Addit. Manuf. 22 (2018) 672–686.
[16] P.F. Jiang, X.R. Li, X.M. Zong, X.B. Wang, Z.K. Chen, H.X. Yang, C.Z. Liu, N.K. Gao, Z.H. Zhang, Multi-wire arc additive manufacturing of Ti basic heterogeneous alloy: effect of deposition current on the microstructure, mechanical property and corrosion-resistance, J. Alloys Compd. 920 (2022), 166056.
[17] P.F. Jiang, X.R. Li, X.M. Zong, X.B. Wang, Z.K. Chen, C.Z. Liu, N.K. Gao, Z. H. Zhang, Microstructure and mechanical properties of Ti basic bionic gradient heterogeneous alloy prepared by multi-wire arc additive manufacturing, J. Alloys Compd. 926 (2022), 166813.
[18] P.F. Jiang, M.H. Nie, X.M. Zong, X.B. Wang, Z.K. Chen, C.Z. Liu, J.Z. Teng, Z. H. Zhang, Microstructure and mechanical properties of TC4/NiTi bionic gradient heterogeneous alloy prepared by multi-wire arc additive manufacturing, Mater. Sci. Eng., A 866 (2023), 144678.
[19] Y. Tian, X. Chen, Y. Cai, Z. Luo, M. Chen, X. Zhang, J. Li, J. Han, Microstructure and properties of a Ni–Ti–Cr–Mo–Nb alloy fabricated in situ by dual-wire arc additive manufacturing, Mater. Sci. Eng., A 853 (2022), 143740.
[20] W. Zhou, C. Shen, X. Hua, Y. Zhang, L. Wang, J. Xin, F. Li, Twin-wire directed energy deposition-arc of Ti–48Al–2Cr–2Nb alloy: feasibility, microstructure, and tensile property investigation, Mater. Sci. Eng., A 850 (2022), 143566.

[21] A. Bulla, K. Wu, C. Shen, Influence of local thermal cycle on the lattice and microstructure evolution of twin-wire directed energy deposition-arc fabricated equiatomic NiTi alloy, Mater. Sci. Eng., A 862 (2023), 144462.
[22] I. Shishkovsky, N. Kakovkina, V. Sherbakov, Graded layered titanium composite structures with TiB_2 inclusions fabricated by selective laser melting, Compos. Struct. 169 (2017) 90–96.
[23] R. Wang, D. Gu, K. Lin, C. Chen, Q. Ge, D. Li, Multi-material additive manufacturing of a bio-inspired layered ceramic/metal structure: formation mechanisms and mechanical properties, Int. J. Mach. Tool Manufact. 175 (2022), 103872.
[24] P. Kah, R. Suoranta, J. Martikainen, C. Magnus, Techniques for joining dissimilar materials: matals and polymers, Rev. Adv. Mater. Sci. 36 (2014) 152–164.
[25] M. Piao, S. Miyazaki, K. Otsuka, N. Nishida, Effects of Nb addition on the microstructure of Ti-Ni alloys, Mater. Trans., JIM 33 (1992) 337–345.
[26] P.F. Jiang, C.H. Zhang, S. Zhang, J.B. Zhang, J. Chen, Y. Liu, Microstructure evolution, wear behavior, and corrosion performance of alloy steel gradient material fabricated by direct laser deposition, J. Mater. Res. Technol. 9 (2020) 11702–11716.
[27] P.F. Jiang, C.H. Zhang, S. Zhang, J.B. Zhang, J. Chen, H.T. Chen, Additive manufacturing of novel ferritic stainless steel by selective laser melting: role of laser scanning speed on the formability, microstructure and properties, Opt Laser. Technol. 140 (2021), 107055.
[28] X. Zhou, Y. Chen, Y. Huang, Y. Mao, Y. Yu, Effects of niobium addition on the microstructure and mechanical properties of laser-welded joints of NiTiNb and Ti6Al4V alloys, J. Alloys Compd. 735 (2018) 2616–2624.
[29] Y. Yin, W. Kou, Y. Zhao, H. Yang, W. Zeng, Hierarchical transition structure induced by gradient composition distribution in layered Ti-TiNb alloy, Scripta Mater. 219 (2022), 114854.
[30] X. Cui, S. Zhang, Z.Y. Wang, C.H. Zhang, C.L. Ni, C.L. Wu, Microstructure and fatigue behavior of 24CrNiMo low alloy steel prepared by selective laser melting, Mater. Sci. Eng., A 845 (2022), 143215.
[31] F. An, L. Zhang, J. Ning, B. Zhang, Z. Sun, S.J. Na, Influence of annealing on the microstructure and Charpy impact toughness of wire arc additive manufactured Ti5111 alloy, Mater. Sci. Eng., A 860 (2022), 144255.
[32] Z. Li, Y. Cui, L. Wang, H. Zhang, Z. Liang, C. Liu, D. Du, An investigation into Ti-22Al-25Nb in-situ fabricated by electron beam freeform fabrication with an innovative twin-wire parallel feeding method, Addit. Manuf. 50 (2022), 102552.
[33] L. Xue, J. Xiao, Z. Nie, F. Hao, R. Chen, C. Liu, X. Yu, C. Tan, Dynamic response of Ti-6.5Al–1Mo–1V–2Zr-0.1B alloy fabricated by wire arc additive manufacturing, Mater. Sci. Eng., A 800 (2021), 140310.
[34] X. Tang, S. Zhang, X. Cui, C. Zhang, Y. Liu, J. Zhang, Tribological and cavitation erosion behaviors of nickel-based and iron-based coatings deposited on AISI 304 stainless steel by cold metal transfer, J. Mater. Res. Technol. 9 (3) (2020) 6665–6681.
[35] W. Li, M. Li, Y. Yang, Q. Wei, D. Cai, J. Liu, C. Yan, Y. Shi, Enhanced compressive strength and tailored microstructure of selective laser melted Ti-46.5Al-2.5Cr-2Nb-0.5Y alloy with different boron addition, Mater. Sci. Eng., A 731 (2018) 209–219.
[36] X. Cui, S. Zhang, C. Wang, C.H. Zhang, J. Chen, J.B. Zhang, Effects of stress-relief heat treatment on the microstructure and fatigue property of a laser additive manufactured 12CrNi2 low alloy steel, Mater. Sci. Eng., A 791 (2020), 139738.
[37] Y. Wu, X. Qin, C. Wang, L. Zhou, Influence of phosphorus on hot deformation microstructure of a Ni-Fe-Cr based alloy, Mater. Sci. Eng., A 768 (2019), 138454.
[38] J.J.S. Dilip, G.D.J. Ram, T.L. Starr, B. Stucker, Selective laser melting of HY100 steel: process parameters, microstructure and mechanical properties, Addit. Manuf. 13 (2017) 49–60.
[39] Y. Chen, K. Zhang, J. Huang, S.R.E. Hosseini, Z. Li, Characterization of heat affected zone liquation cracking in laser additive manufacturing of Inconel 718, Mater. Des. 90 (2016) 586–594.
[40] D. Xu, M. Zhou, Y. Zhang, S. Tang, Z. Zhang, Y. Liu, B. Tian, X. Li, Y. Jia, A. A. Volinsky, et al., Microstructure and hot deformation behavior of the Cu-Sn-Ni-Zn-Ti(-Y) alloy, Mater. Char. 196 (2023), 112559.
[41] Y.F. Tao, J. Li, Y.H. Lv, L.F. Hu, Effect of heat treatment on residual stress and wear behaviors of the TiNi/Ti_2Ni based laser cladding composite coatings, Opt Laser. Technol. 97 (2017) 379–389.
[42] P. Liu, L. Cheng, Y.W. Zhang, Interface toughness under combined mode I, II and III loadings, Scripta Mater. 44 (2001) 487–492.
[43] B. Wu, Z. Qiu, Z. Pan, K. Carpenter, T. Wang, D. Ding, S.V. Duin, H. Li, Enhanced interface strength in steel-nickel bimetallic component fabricated using wire arc additive manufacturing with interweaving deposition strategy, J. Mater. Sci. Technol. 52 (2020) 226–234.
[44] Z. Liu, Z. Du, H. Jiang, X. Zhao, T. Gong, X. Cui, J. Cheng, F. Liu, W. Chen, Controlling the microstructure and fracture toughness of the Ti–5Al–5Mo–5V–1Cr–1Fe alloy by multiple heat treatments, J. Mater. Res. Technol. 17 (2022) 2528–2539.